Effect of plastic deformation on the spreadability of cohesive powder in the spreading process

Wenguang Nan [a],[b],[*], Md Arifur Rahman [a], Lanzhou Ge [a], Zhonggang Sun [c]

[a] School of Mechanical and Power Engineering, Nanjing Tech University, Nanjing 211816, China
[b] Faculty of Engineering and Physical Sciences, University of Leeds, Leeds LS2 9JT, UK
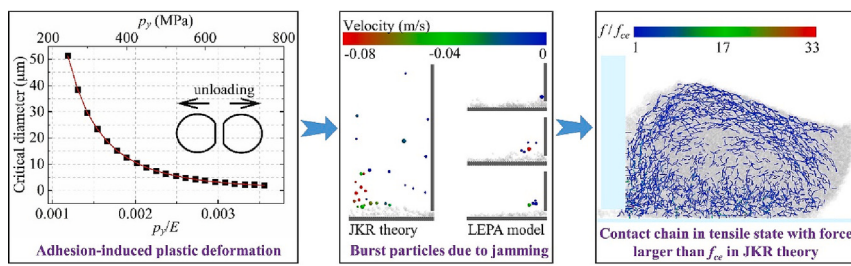[c] College of Materials Science and Engineering, Nanjing Tech University, Nanjing 211816, China

HIGHLIGHTS

- Mechanical jamming of particles is inhibited by plastic deformation.
- Particle flowability within the heap is reduced by the decrease of *CY* number.
- Plastic deformation could be induced by mechanical jamming at narrow gap.
- Better spreadability could be obtained if plastic deformation is involved.
- Effect of plastic deformation is not the same as increasing particle surface energy.

GRAPHICAL ABSTRACT

ARTICLE INFO

ABSTRACT

Powder spreadability is critical to particle spread layer and thus the quality of final product in powder-based additive manufacturing. In this work, the effect of plastic deformation on the spreadability is investigated, in which particle jamming, particle dynamics within the heap, and spread layer are analysed. The results show that under the effect of plastic deformation, mechanical jamming at narrow gap is significantly reduced, and flowability of particles becomes worse. Large tensile force of contacts could be induced by jamming even when cohesion yield number (*CY*) is larger than 1. Better spreadability could be obtained if plastic deformation is involved, due to less jamming. However, if the plastic deformation of particles within the heap is too large, spreadability would be significantly reduced, due to worse flowability. The results also clarified that the effect of plastic deformation on powder spreadability could not be simply replaced by adding extra surface energy to the particles.

1. Introduction

Additive manufacturing (AM) or 3D printing technology has revolutionized the design and manufacturing industries removing the barrier in achieving complex design and process with inexpensive tools and shortened process time [1–4]. A wide range of materials have been used in AM providing flexibility in the manufacturing process which makes AM more desirable amongst the others [5–7]. Broadly, AM techniques could be classified into two parts: powder-based process and liquid-based process. In the powder-based process, micrometre sized fine and dry powders are spread in thin layers by a spreading blade or a roller [8–10]. Then the spread layer is locally heated by a radiative energy

beam to melt or sinter the layer, and this process is repeated until the production of the final part is finished. However, powders show peculiar flow characteristics during spreading such as mechanical arching and transient jamming, which leads to defective final products with poor mechanical performance [11–13]. Although previous studies have quantified the microscopic behaviour of bulk powder, there is still a lack of clear understanding, as reviewed by Ghadiri et al. [14]. Therefore, there are still many challenges in this research domain, from realistic quantitative and predictive simulations to experimental validation of many-particle systems as well as transitions from microscopic contact properties to macroscopic flow behaviour.

In recent years, discrete element method (DEM) has been used to explore the fundamentals of powder spreading in AM which provides information of individual particles allowing to conduct studies in a controlled manner [15–24]. In context of the definition of powder spreadability, no detailed study is found until Nan et al. [13] and Ghadiri et al. [14]. They firstly proposed the idea of spreadability as the ability of the powder to spread uniformly as a thin layer which is a few multiples of particle diameter thick without empty patch formation and agglomeration. Furthery, Snow et al. [25] described the spreadability metrices by fraction of powder coverage in the powder bed, mass deposition rate, the average avalanching angle of the heap before the blade and the rate of change in the avalanching angle. In addition, many researchers have also made corresponding research on the influencing factors of spreading process. Parteli and Pöschel [26] and Haeri et al. [27] discovered that increasing spreader speed and using wider ranged particle size distribution could result in poor powder bed with higher surface roughness. Yao et al. [28] studied the influence of blade speed and gap height on the quality of the spread powder bed. They found that the high quality of powder bed can be effectively obtained by properly adjusting the spread parameters. Chen et al. [29,30] found that rolling and sliding friction coefficients between particles and percolation effect in powders with a bimodal particle size distribution had significant impacts on the powder bed, where the mechanical properties of the spherical particles were tuned. Mussatto et al. [31] analysed the influence of powder morphology, spreading speed and powder layer thickness on powder spreadability through experiments, but did not put forward a standard to compare the relative spreadability of different powders. Le et al. [32] obtained the high-precision morphology of powder layer by scanning technology and studied the spreadability of powder based on the morphology of powder layer. Zhang et al. [33] studied the spreading process of nylon powder by roller and blade. By dividing the powder flow area into several bins and analysing the particle flow behaviour and powder layer density in each area, they comprehensively evaluated the spreadability of these two spreading methods, and considered that roller-spreading could lead to better spreadability. Shaheen et al. [20] analysed the influence of material and process parameters on spreadability, and found that irregular particles, rough particle surfaces and high interfacial cohesion mostly resulted in poor spreadability. Finally, particle size was concluded as a crucial spreadability parameter by He et al. [34], they discovered that an ideal layer could either be obtained by small particle size with weak surface cohesiveness or large particles with moderate surface cohesiveness. However, particles tend to be more cohesive as the particles become smaller which leads to a sparse and non-uniform spread layer. According to Nan et al. [35], particles with size below a critical value could be affected by adhesion-induced plastic deformation or jump-in induced plastic deformation, which increase the particle's cohesiveness even more and become an obstacle to form ideal powder bed. Therefore, in depth study about the effect of plastic deformation during powder spreading is necessary so that the spreadability could be improved.

In this paper, we report the effects of plastic deformation on the spreadability of cohesive powder based on numerical simulation using Discrete Element Method (DEM). A heap of cohesive powder is subjected to a translational motion of a vertical blade with a gap allowing particle to spread and form a thin layer. The results from the cases with and without considering plastic deformation are compared, including the spread layer, jamming and particle dynamics in the heap. This work highlights the importance of plastic deformation on spreadability of cohesive powder, which could provide a good reference for powder-based AM.

2. Methods

2.1. Contact model

Particle dynamics in the spreading process are modelled by Discrete Element Method (DEM), in which particle motion is tracked individually by solving Newton's laws of motion and calculating the contact force for each contact pair [36,37]. For powder used in AM, the contact could be elasto-adhesive, or elasto-plastic and adhesive, as shown in Fig. 1. For the first, as the particles tend to stick to each other, additional work is needed to separate them, but the deformation could be fully recovered after detachment. It could be well described by Hertz-Mindlin model with Johnson-Kendall-Roberts (JKR) theory [38]. For the latter, only partial deformation could be recovered, and permanent deformation with flattened area is retained during detachment, which makes the contact behave more cohesively. It could be described by a linear model recently developed by Nan et al. [35]. The schematics of both models are shown in Fig. 2, with key information described below, and more details could be referred to Nan et al. [35].

In Hertz-Mindlin model with JKR theory, the normal force F_n is given as:

$$F_n = \frac{4E^* a^3}{3R^*} - \sqrt{8\pi \Gamma E^* a^3} \tag{1}$$

where Γ is the interfacial surface energy; E^* is the equivalent Young's modulus, given as $1/E^* = (1- \nu_1^2)/E_1 + (1 - \nu_2^2)/E_2$, where ν is the Poisson's ratio; R^* is the effective radius, given as $R^* = R_1 R_2/(R_1+ R_2)$; a is the contact radius, which could be calculated from overlap α. The maximum pull-off force f_{ce} in Fig. 2 is independent of the loading process, given as:

$$f_{ce} = 1.5\pi \Gamma R^* \tag{2}$$

In the linear elasto-plastic and adhesive contact model (LEPA), the normal force f is given as:

$$f = \begin{cases} min(f_e, f_p) & \alpha > \alpha_{cp} \\ f_c & \alpha_{fp} \leq \alpha \leq \alpha_{cp} \\ 0 & \alpha < \alpha_{fp} \parallel cs = 0 \end{cases} \tag{3}$$
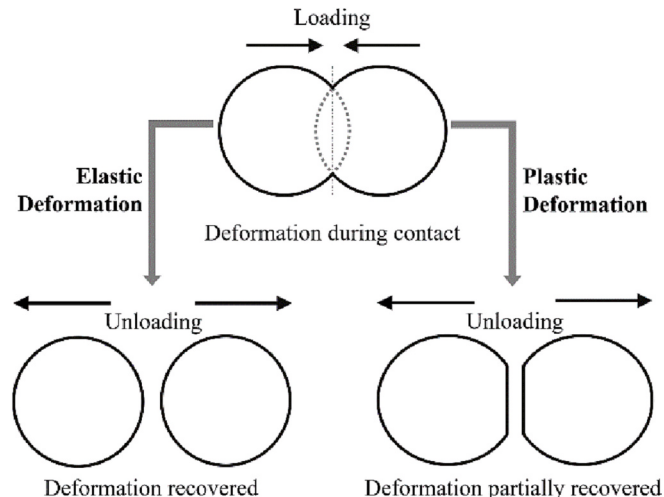

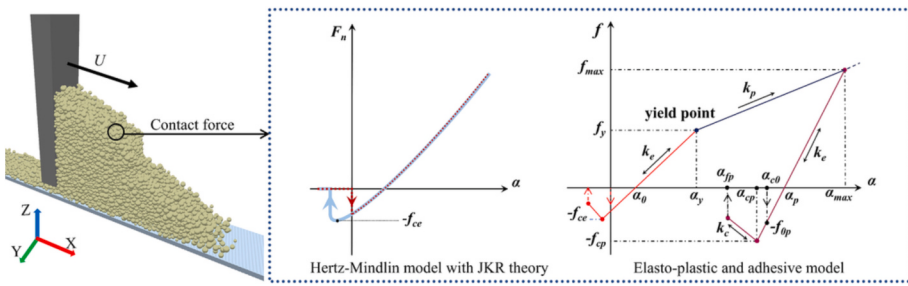**Fig. 1.** Contacts with and without plastic deformation.

Fig. 2. Schematic of particle spreading process in simulation and contact model.

where α_{cp} is the overlap where the maximum pull-off force f_{cp} is reached; α_{fp} is the overlap where the particles in contact are detached; cs is a parameter describing the contact state; f_e, f_p and f_c are the forces, given as:

$$f_e = k_e(\alpha - \alpha_p) \tag{4}$$

$$f_p = f_y + k_p(\alpha - \alpha_y) \tag{5}$$

$$f_c = -f_{cp} + k_c(\alpha_{cp} - \alpha) \tag{6}$$

where α_p is the overlap after yielding where the normal force is zero; k_e is the elastic stiffness after yielding; f_y is the yield force; k_p is the plastic stiffness; α_y is the overlap at the yielding point; k_c is the stiffness when the overlap is less than α_{cp}. The maximum pull-off force f_{cp} in Fig. 2 is given as:

$$\frac{f_{cp}}{f_{ce}} = \frac{-A + \sqrt{A^2 + 4\frac{k_e}{k_{el}}\left(\frac{\alpha_p}{\alpha_0}A + 1\right)}}{2} \tag{7}$$

$$\frac{k_e}{k_{el}} = \sqrt{\frac{\alpha_{max}}{\alpha_y}} \tag{8}$$

where A is constant for each contact pair; k_{el} and α_0 are the parameters before yielding, corresponding to k_e and α_p, respectively; α_{max} is the maximum overlap with force f_{max} at which the unloading commences, and it would be only immediately updated and equal to the normal overlap when the contact is yielded again, to prepare for the possible unloading process in the next time step. During the reloading stage, the contact could only be re-established at $\alpha = \alpha_{c0}$ with an initial value of $-f_{0p}$. Yield point and plastic stiffness could be calculated based on the yield contact pressure. Compared to Hertz-Mindlin model with JKR theory, yield contact pressure p_y is needed to be additionally provided in LEPA model. It should be noted that for the contact before yielding, LEPA model could be simplified into the linear version of Hertz-Mindlin model with JKR theory, in which same cohesive behaviour of an individual particle could be predicted.

2.2. Critical particle size

For a given material, the effect of plastic deformation must be accounted if the particle size is below the critical value. Nan et al. [35] proposed a non-dimensional number to quantify the critical particle radius, below which the attractive force itself could induce plastic deformation (i.e. adhesion-induced plastic deformation or jump-in induced plastic deformation), given as:

$$CY = \frac{p_y{}^3 R}{E^2 \Gamma} \tag{9}$$

For a given material (i.e. p_y, E, Γ is fixed), below the critical particle size ($CY = 1$), the smaller the particle size, the particle behaves more cohesively than the one predicted by JKR theory. For powder used in

AM, the data of the surface energy of an individual particle is usually not available in the literature, in which the surface energy in most simulations was artificially evaluated to get the same bulk flowability (i.e. repose angle of the heap) as the experiment. According to this fact, the critical particle diameter is only examined for gas-atomised 316L stainless steel powder, the properties of which are experimentally characterised by Nan et al. [13]. Fig. 3 shows the variation of critical particle size with yield contact pressure p_y, where $E = 211$ GPa and $\Gamma = 9$ mJ/m^2 from Nan et al. [13] is used. The critical particle size is calculated based on Eq. (9), where $CY = 1$ is specified. In real AM process, the diameter of 316L stainless steel powder is usually in the range of 15–53 μm or <10 μm. It could be found that the range of critical particle size and particle size distribution (PSD) of powder used in reality is overlapped. For example, considering the fact that the yield stress of 316L stainless steel is usually 200–300 MPa, resulting in contact pressure about 320–480 MPa and p_y/E around 0.0015–0.0023, the critical particle diameter would be about 24.5–7.2 μm, where the ratio of the contact pressure to yield stress is about 1.6 based on the work of Nan et al. [35]. Therefore, for fine powder used in AM process, the effect of plastic deformation should be considered. Of course, for powder above the critical size, the plastic deformation may be also induced by the heap weight or the blade/base force. The modeling of the spreading process of very fine powder is too time-consuming, due to billions of particles and nanosecond time-step. Therefore, large particles but with low yield contact pressure are used to highlight the effect of plastic deformation on the powder spreading process, where the cases with CY number larger and smaller than 1 are both included, as described in Section 2.3.
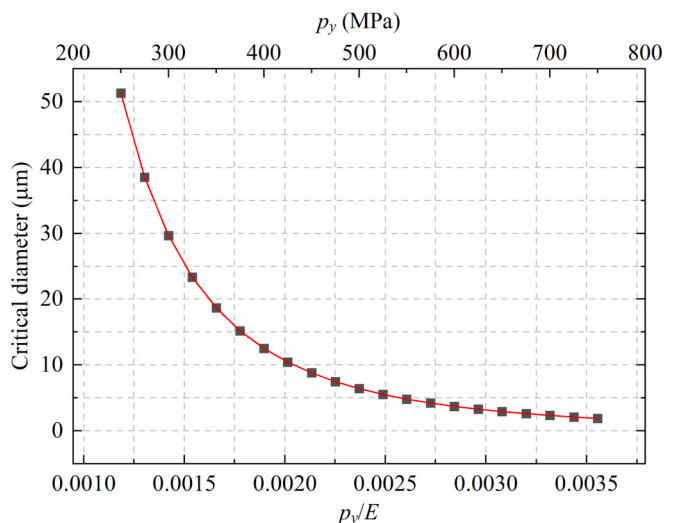

Fig. 3. Variation of critical particle size (beyond which adhesion-induced plastic deformation could occur) with yield contact pressure, where $E = 211$ GPa and $\Gamma = 9$ mJ/m^2 from Nan et al. [13] is used.

2.3. Simulation conditions

The particulate system includes a spreading blade and a rough base, as shown in Fig. 2. Total 24 kinds of particles are used, for which the physical properties of particles are shown in Table 1 [13], and the number-based equivalent-circle diameters D_{10}, D_{50} and D_{90} are 20 μm, 32 μm and 45 μm, respectively. The dimensions of the simulation domain in the spreading and lateral directions are $400D_{90}$ and $10D_{90}$, respectively. The front and rear boundaries of the simulation domain are periodic. The base is of the same length (X direction) and width (Y direction) as the simulation domain, and it is made up of clumped cylinders with axes along the Y direction. All the simulations are carried out in two steps: heap generation and particle spreading. The initial heap for spreading is produced by poured packing method (total mass is approximately 3 mg). At the beginning of the spreading process, the spreading blade is lifted (along Z axis) to maintain a gap height of δ between the blade and the layering base, then quickly accelerates for a short duration of time to reach a constant speed of $U = 0.08$ m/s in the spreading direction, according to the work of Nan et al. [39]. The spreading blade moves forward at this constant speed until a layer with the length about $320D_{90}$ is formed.

To investigate the effect of plastic deformation on powder spreading process, six cases with and without considering plastic deformation are used, i.e. cases J1-J3, and cases L1-L3, as shown in Table 2. For each case, two gap heights are used, i.e. $\delta = 2.2D_{90}$ and $\delta = 1.5D_{90}$. In cases J1-J3, only the surface energy is varied. Cohesion number and bond number are used to quantify the effect of surface energy on the adhesive behaviour of an individual particle [40], given as:

$$Bo = \frac{9}{2}\frac{\Gamma}{\rho g D_{90}^2} \tag{10}$$

$$Coh = \frac{1}{\rho g}\left(\frac{\Gamma^5}{E^2 R^8}\right)^{1/3} \tag{11}$$

In cases L1-L3, the surface energy is the same as case J1, and only the yield contact pressure is varied. The range of yield contact pressure in cases L1-L3 is selected to get similar repose angles as cases J1-J3, and two classes of CY number, i.e. $CY > 1$ for case L1 and $CY < 1$ for cases L2 & L3, as shown in Table 2. Fig. 4 shows the snapshots of the initial heap before spreading. With the increase of surface energy or the decrease of yield contact pressure, the repose angle increases, resulting in worse flowability. Meanwhile, cases J1 and L1 have similar repose angle, which is also true for cases J2 and L2, cases J3 and L3.

3. Results

3.1. Particle jamming

Fig. 5 shows the snapshots of burst particles, where the burst particles are coloured by their velocity in the spreading direction. Here, the burst particles are referred to the particles behind the blade, but their centre of mass is higher than $\delta + D_{90}$. In case J1, several burst particles have negative velocity with the magnitude close to blade speed U, which could give the particles enough momentum to fly further away from the blade and reach a higher elevation. For example, the highest position of burst particles in case J1 could be >20 times of the gap height. The nature of bust particles in cases J2 and J3, is similar to that of case J1, but the particles are relatively larger and stay at a much lower elevation.

Table 1
Physical properties of particles.

Parameters	Value	Parameters	Value
Particle diameter, D_{90} (μm)	45	Poisson ratio, ν	0.3
Particle density, ρ (kg/m³)	7980	Friction coefficient, μ	0.5
Young's modulus, E (GPa)	2.11	Restitution coefficient, e	0.64

Table 2
Parameters in cases J1-J3 and cases L1-L3.

Cases	Surface energy Γ (mJ/m²)	Yield pressure P_y (MPa)	Cohesion number*	Bond number*	CY number*
J1	1.4	–	0.0003	40	–
J2	11.2	–	0.01	318	–
J3	20	–	0.028	568	–
L1	1.4	50	–	–	451
L2	1.4	5	–	–	0.45
L3	1.4	2.5	–	–	0.056

* Cohesion number and Bond number is calculated from surface energy, while CY number is calculated from yield contact pressure.
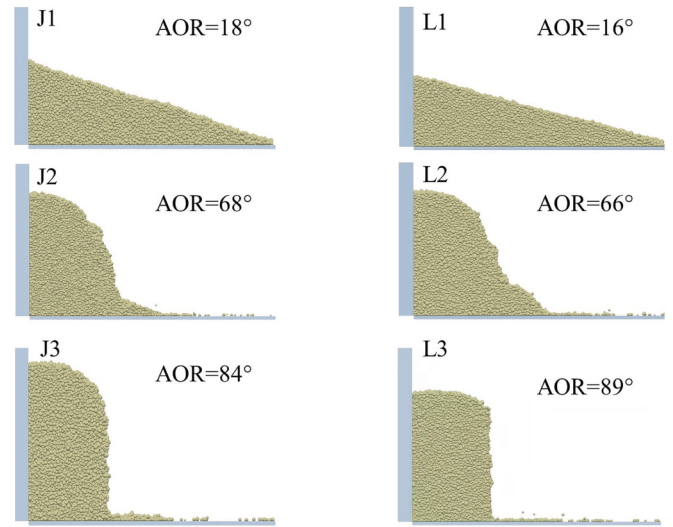

Fig. 4. Snapshots of the initial heap before spreading, where angle of repose (AOR) is included.

Meanwhile, the velocity of burst particles in cases J2 and J3 is much lower, and some burst particles tend to be adhered to the blade under the effect of strong cohesion (i.e. large cohesion number and bond number).

Compared to cases J1-J3, the behaviour of burst particles in cases L1 & L2 is much different. There are only a few of burst particles in cases L1 and L2, with vertical locations close to the base. The frequency of the formation of burst particles in cases L1 & L2 is also much less than that of J1, which could be observed from the video recording of the spreading process (not shown here for simplicity). This could be further illustrated by the time-averaged number of burst particles, as shown in Fig. 6. At the gap height of $\delta/D_{90} = 2.2$, almost no burst particles could be found, expect for case J2. At the gap height of $\delta/D_{90} = 1.5$, with the increase of the cohesion number or the decrease of CY number, the average number of burst particles decreases. Meanwhile, compared to cases J1-J3, the number of burst particles in cases L1 and L2 is significantly reduced, which is consistent with Fig. 5. It suggests that the mechanical jamming is much weaker due to plastic deformation.

Fig. 7 shows the variation of the total force on the blade and base with time, where the force is normalised by the total weight of the heap Mg. To avoid the small fluctuations due to the heap weight and highlight the effect of mechanical jamming, the value of force with magnitude <$2Mg$ is neglected and not shown in the figure. Here, only the cases with the gap height of $1.5D_{90}$ are shown, as the force at the gap height of $2.2D_{90}$ is always <$2Mg$ and not shown here for simplicity. As shown in Fig. 7(a), the data points are sparse with a few of very large value, in case J1, indicating the occurrence of mechanical jamming due to narrow gap. With the increase of cohesion number, i.e. cases J2 and J3, the data points are denser, and more data points have a large value. For example, force with the magnitude around $500Mg$ could be found at several time
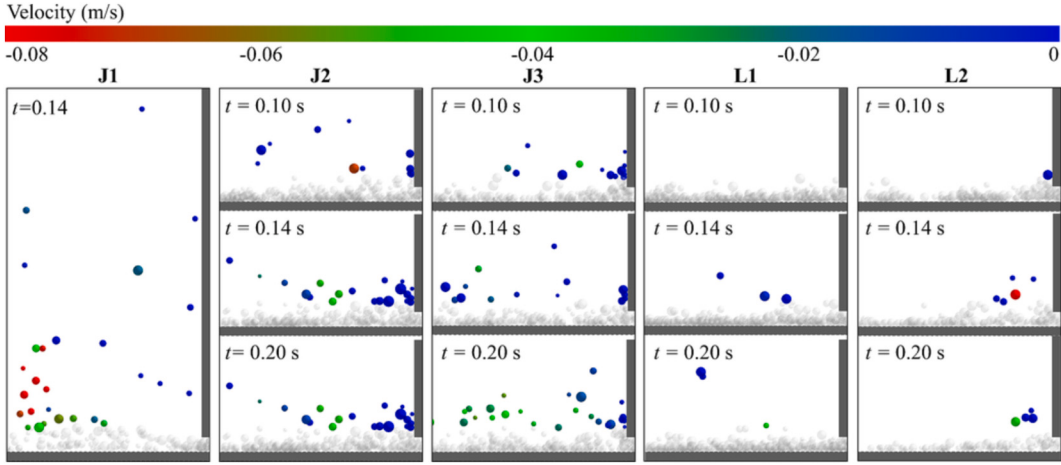
Fig. 5. Snapshots of burst particles at the gap height of $\delta/D_{90} = 1.5$, where the burst particles are coloured by their velocity in the spreading direction, and the blade is referred to the vertical rectangle in dark grey.
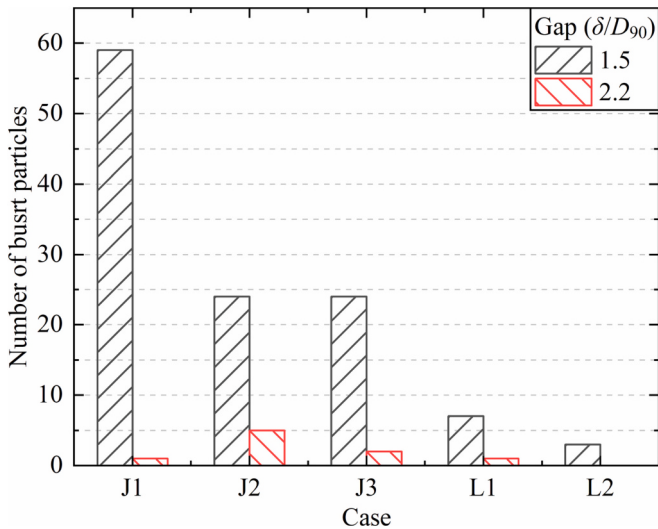

Fig. 6. Time-averaged number of burst particles.

points in cases J2 and J3, while it could only be found around $t = 0.17$ s in case J1. It suggests that proper cohesion would promote the strength of mechanical jamming. As shown in Fig. 7(b), compared to cases J1-J3, the magnitude of data points in cases L1-L3 is much smaller. For example, the maximum force in cases L1 and L2 is only around $100Mg$ and $20Mg$, respectively, and most data points in case L2 are only a little larger than $2Mg$. Compared to the force on the blade, the downward force on the base, as shown in Fig. 7(c-d), is much larger, but the trend is similar, i.e. the force in cases L1-L3 is much smaller than that of cases J1-J3. These results suggest that both the frequency and strength of mechanical jamming is significantly reduced by the plastic deformation for the cases with narrow gap. It is mainly due to that the particles after plastic deformation become less resistant to the blade shearing action.

3.2. Particle dynamics within the heap

Fig. 8 shows the contact chain in case L2, which is coloured by the magnitude of the contact force. Here, only the contacts in a tensile state and with force magnitude larger than $f_{ce} = 1.5\pi R^* \Gamma$ is shown for better illustration, where $R^* = D_{90}/4$ assuming two contact particles with diameter of D_{90}. It shows that the tensile force is not homogenous within the heap. The contacts close to the blade have a larger tensile force, which is mainly due to the effect of blade shearing. It also shows that the

tensile force could be larger than the value predicted by JKR theory, i.e. $f_{ce} = 1.5\pi R^* \Gamma$, which is intuitively expected as plastic deformation could be easily induced by the jump-in attractive force for $CY < 1$ in case L2, as described in Section 2.2. Therefore, different to case J1, where the tensile force is not larger than $f_{ce} = 1.5\pi R^* \Gamma$, the cohesion intensity of an individual particle in case L2 is in a dynamic state and varies significantly with the external load.

Fig. 9 shows the variation of the maximum value of the tensile force with time for all particle-particle contacts in front of the blade, where the force is normalised by $f_{ce} = 1.5\pi R^* \Gamma$ with $R^* = D_{90}/4$. For case L1, the force is around f_{ce} at both gap heights, especially for $\delta/D_{90} = 2.2$, indicating that particle-particle contacts are not yielded, and the particles behave as elasto-adhesive. This is mainly due to large CY number in case L1, requiring large external load to yield the contact. With the decrease of CY number, i.e. cases L2 and L3, the time-averaged value of force increases, which is much larger than f_{ce} predicted by JKR theory. The force in cases L2 and L3 mainly fluctuates around the mean value, especially for $\delta/D_{90} = 2.2$. It is interesting that a few of scatters with large value could be found at the gap height of $\delta/D_{90} = 1.5$ in case L1, i.e. the maximum tensile force could jump to about $40f_{ce}$. It is mainly due to the effect of jamming, where the contacts are yielded under the large force caused by jamming, although the CY number is much larger than 1.

To further explore the effects of plastic deformation on powder spreading, the trajectories of particles forming the final layer are analysed. Here, the particles in a cube with a size of $4D_{90} \times 10D_{90} \times 2D_{90}$ in the spread layer at $t = 0.2$ s are tracked backwardly, and their spatial positions are shown in Fig. 10, where the tracked particles are in red colour while other particles are transparent. In case J1, particles cascade along the heap, and then they are dragged and move along the bottom of the heap by the stagnation effect of the rough base. With the increase of the cohesion number, i.e. cases J2 and J3, the initial position of particles becomes lower, and the particles tend to slide along the bottom of the heap, in a simple and straight route. Compared to case J1, the trajectory of case L1 is similar, as the effect of plastic deformation on the flow-ability in case L1 is limited due to large CY number. This is consistent with the maximum tensile force in Fig. 9. However, in case L2, the initial position of particles is very close to each other, and the particles tend to move in the form of cluster.

The effects of plastic deformation on powder flow within the heap could also be analysed by the shear velocity distribution in front of the blade. Here, the region highlighted in the snapshot embedded in Fig. 11, is divided into 11 bins in Z direction with height equal to D_{90}, and the neighbouring bins are overlapped by 50% in Z direction. The variation of time-averaged particle velocity u_x in each bin with height H from the base is illustrated in Fig. 11. In all cases, particle velocity u_x increases
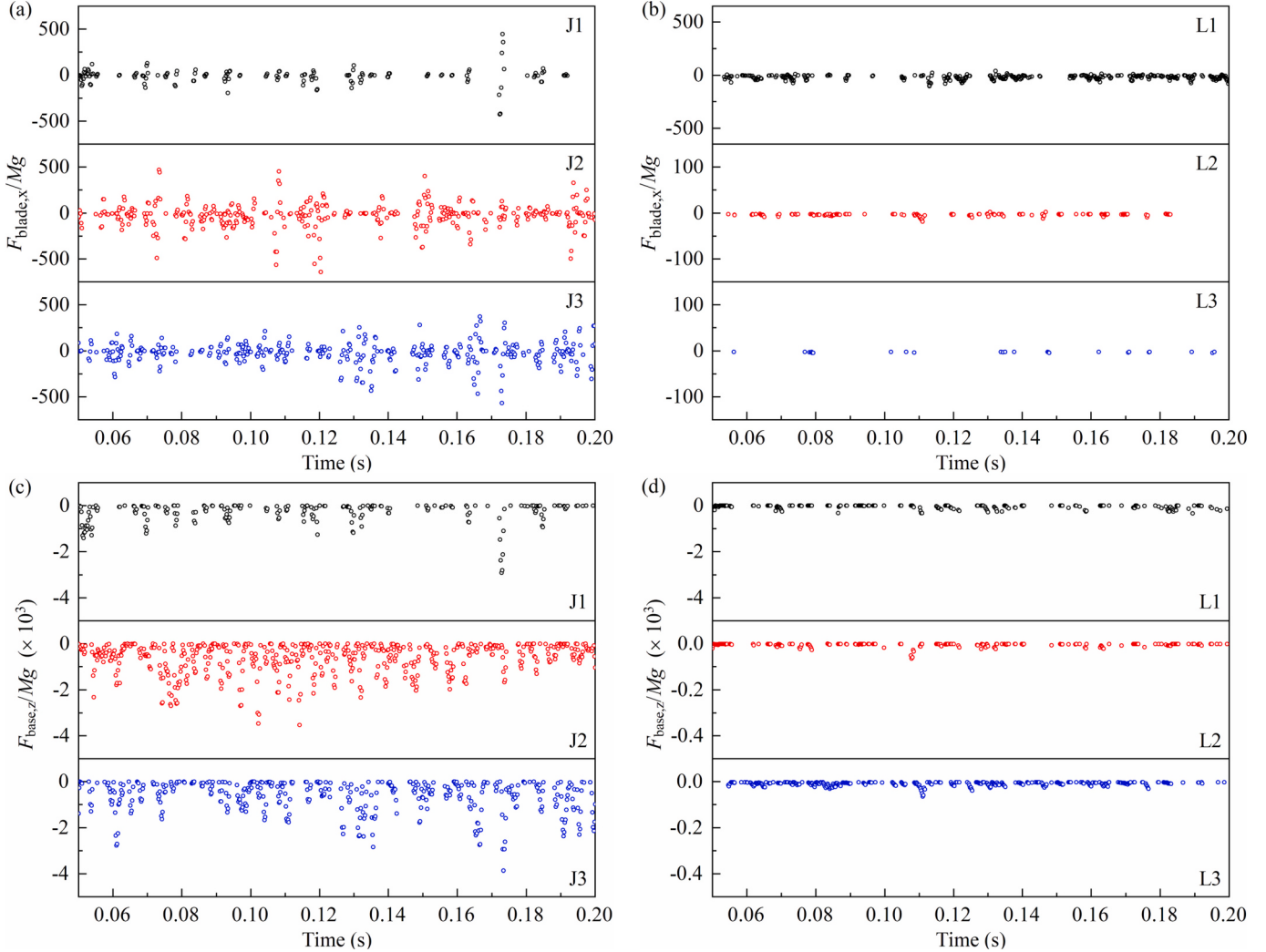
Fig. 7. Variation of force with time in the cases with the gap height of $1.5D_{90}$, (a)-(b): total force on the blade in the spreading direction, (c)-(d): total downward force on the base, where the force is normalised by the total weight Mg of heap in front of the blade, and the data points with magnitude $<2Mg$ are neglected and not shown.
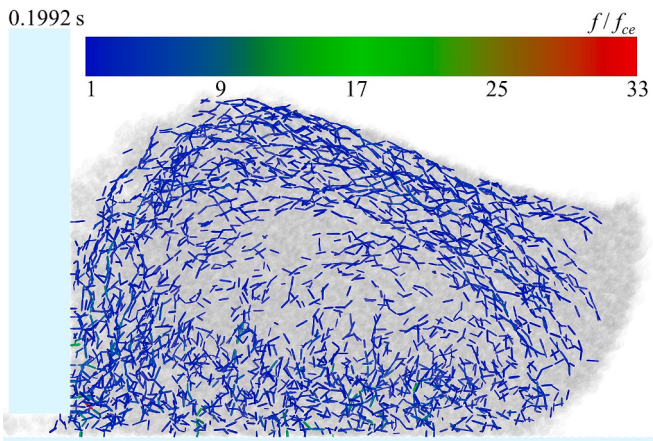

Fig. 8. Contact chain with contacts in tensile state and tensile force larger than $f_{ce} = 1.5\pi R^* \Gamma$, where $R^* = D_{90}/4$ assuming two contact particles with diameter of D_{90}.

with height H and finally reaches a plateau with value equal to blade speed U. For case J1 and L1, their trend is similar at both gaps. With the decrease of CY number, the velocity distribution becomes closer to the blade speed at the bins with H less than gap height. It suggests that the particles tend to be more dragged by the blade shearing action. For case L3, the particle velocity could be larger than $0.9U$ even for the particles in contact with the rough base. Meanwhile, the velocity distribution is not affected by the gap height. These results suggest that the particles within the heap in case L3 move in the form of block.

3.3. Spread layer

Based on the earlier work of Nan et al. [13,41,42] and Ghadiri et al. [14], the spreadability is quantified by three metrics of the particle spread layer, i.e. empty patches, total volume of particles deposited on the rough base, and local volume deviation along the spreading direction. Here, empty patches are referred to the area of the base which is not covered by any particles. Total particle volume of spread layer V_{total} is normalised as:

$$\phi = \frac{V_{total}}{LWD_{90}} \tag{12}$$

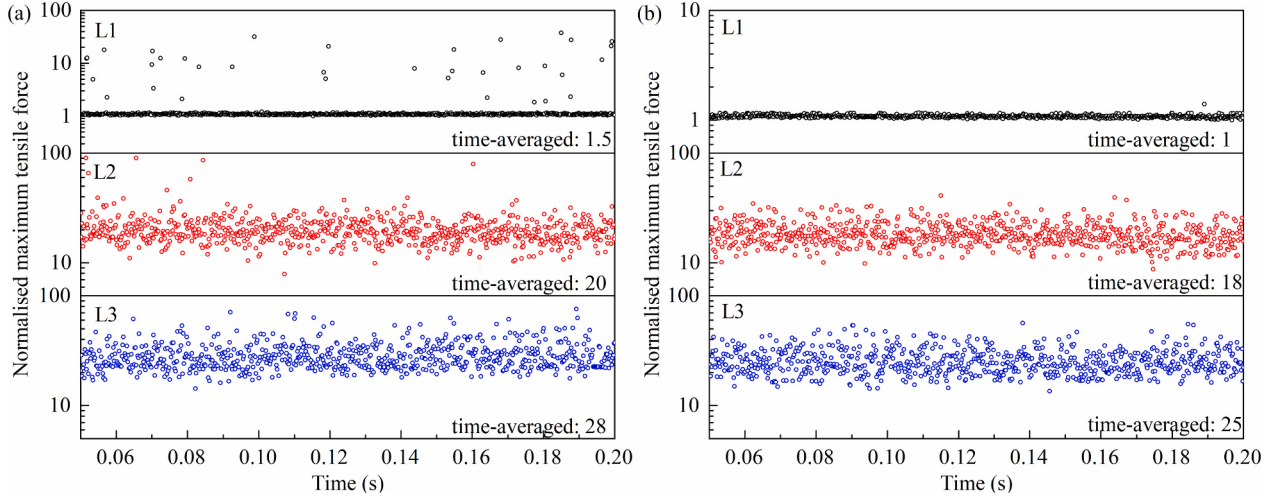where L and W are the length and width of the spread layer, respectively.

Fig. 9. Variation of the maximum value of the tensile force with time for all particle-particle contacts in front of the blade, (a): $\delta/D_{90} = 1.5$ and (b): $\delta/D_{90} = 2.2$, where the force is normalised by $f_{ce} = 1.5\pi R^* \Gamma$ with $R^* = D_{90}/4$.
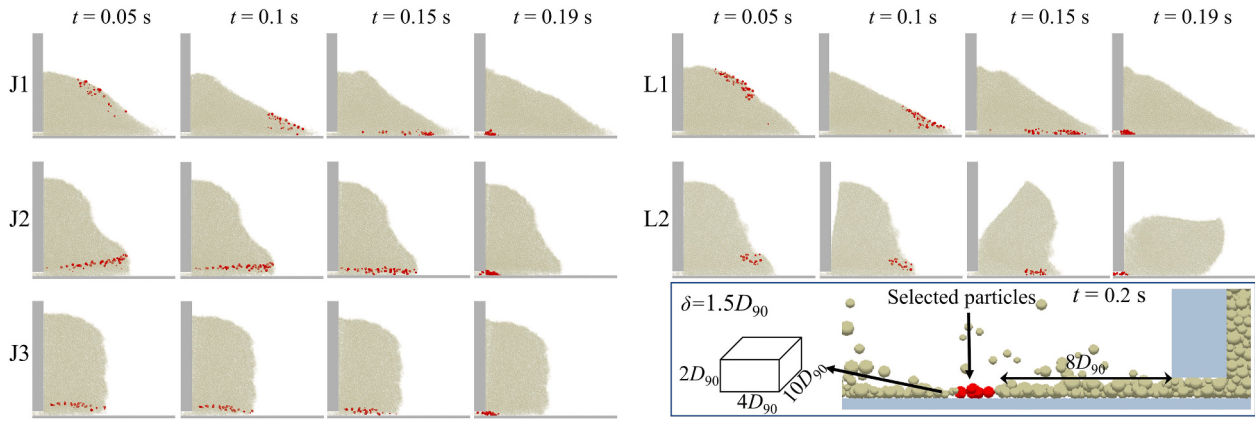

Fig. 10. Snapshots of the spatial positions of the particles in the selected cell which are back-tracked.
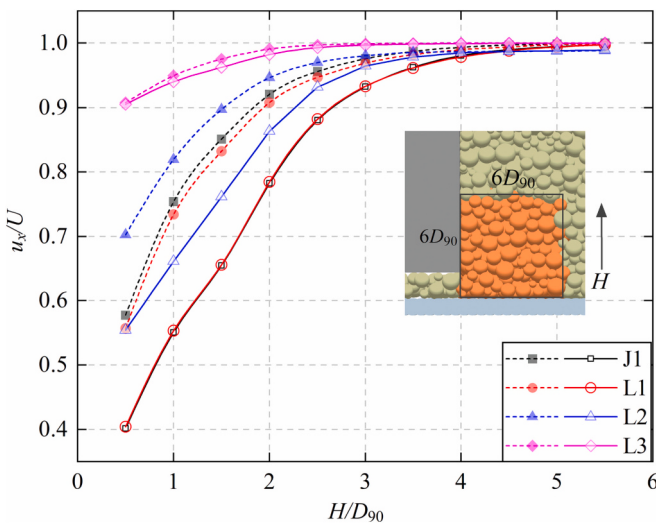

Fig. 11. Variation of averaged particle velocity u_x with the height H of the centre of the bins from the base, where dash line with solid symbol: $\delta/D_{90} = 1.5$, and solid line with open symbol: $\delta/D_{90} = 2.2$.

Local volume deviation SI along the spreading direction is calculated as:

$$SI = \frac{\sum\limits_{i=1}^{N}\left(\frac{|V_{tot,i} - V_{mean}|}{V_{mean}}\right)}{N} \qquad (13)$$

where the spread layer is divided into $N = 20$ bins along spreading direction, and the total particle volume $V_{tot,i}$ is calculated locally for each bin, V_{mean} is the corresponding mean value of $V_{tot,i}$. Lower value of SI indicates more uniform spread layer.

Fig. 12 shows the snapshots of the particle layer after spreading, where particles are coloured by the volume. For case J1, there are a number of empty patches at the gap height of $\delta = 1.5D_{90}$, while the base is almost fully covered by particles at the gap height of $\delta = 2.2D_{90}$. With the increase of cohesion number, more empty patches could be found, especially for case J3, where large empty patches could be obviously found at both gap heights. Compared to case J1, i.e. at the same cohesion number, with the decrease of CY number, there are more and more empty patches. For case L2, large agglomerates are observed in the spread layer, which is different to case J2, although their repose angles of the initial heap are similar. For case L3, particles could even not be spread onto the base like other cases. The worst spreadability of case L3 is mainly due to large additional cohesion caused by plastic deformation, and particles tend to move with the blade like a block.

The ratio of the area of empty patches to that of the base is shown in Fig. 13, which is calculated from the image analysis of the snapshots in
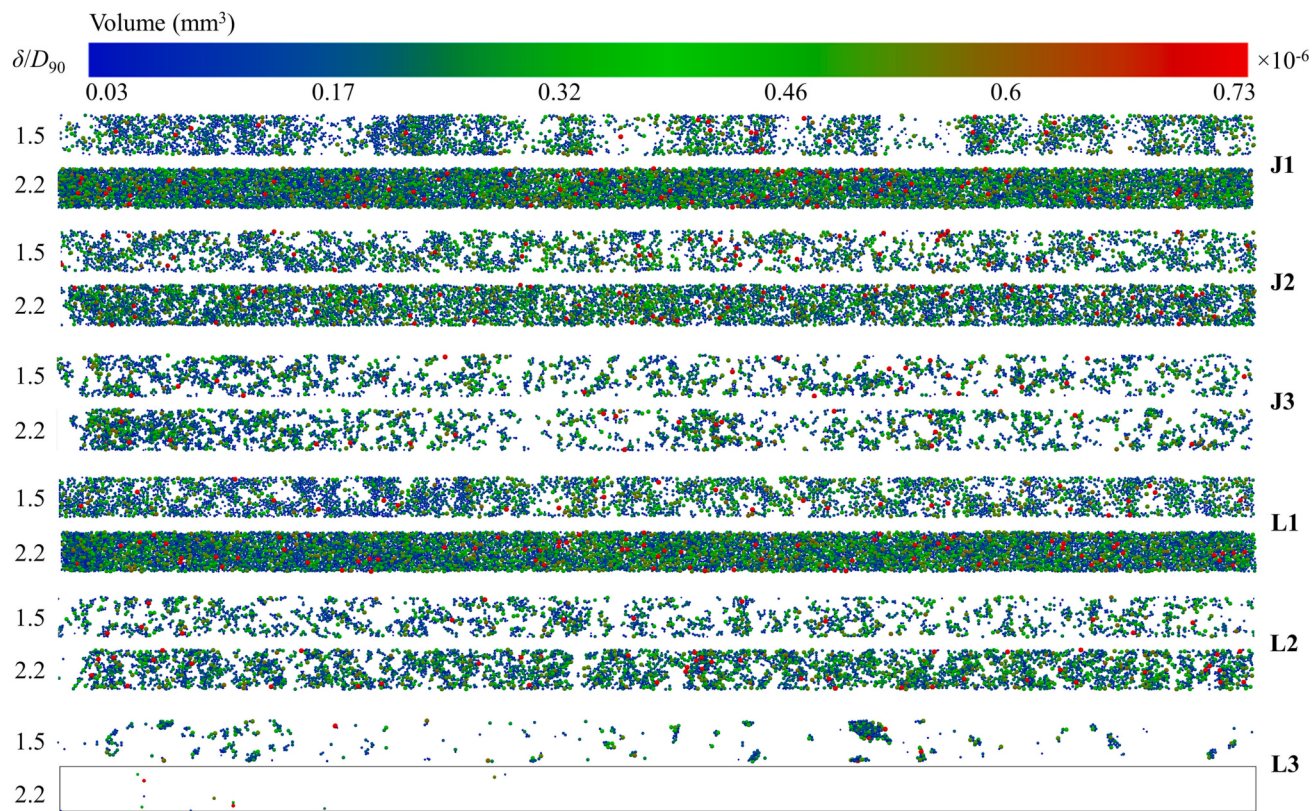
Fig. 12. Snapshots of spread layer, where the particles are coloured based on particle volume and the base is transparent, and two different gap heights are used: $\delta = 2.2D_{90}$ and $\delta = 1.5D_{90}$.
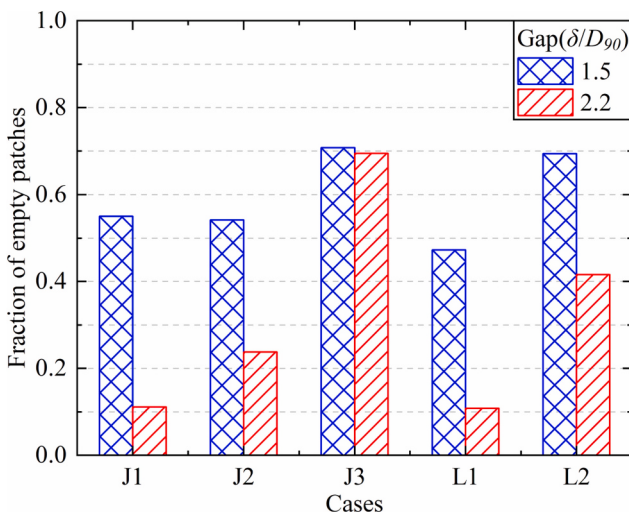

Fig. 13. Fraction of empty patches within the spread layer.

Fig. 14. Total volume of particles within the spread layer.

Fig. 12. Similarly, total normalised volume of particles within the spread layer is shown in Fig. 14. At large gap height of $\delta = 2.2D_{90}$, with the increase of cohesion number or the decrease of CY number, the fraction of empty patches area increases, while the total volume of particles decreases. It suggests that the area ratio of empty patch is directly related to the amount of particles deposited on the base. Thus, large area ratio of empty patches is mainly due to not enough powder flowing through the gap. At small gap height of $\delta = 1.5D_{90}$, the extent of the variation of empty patches area and total particle volume with cohesion number or CY number is much reduced, as the jamming effect is dominant at this condition. Meanwhile, compared to case J1, case L1 has
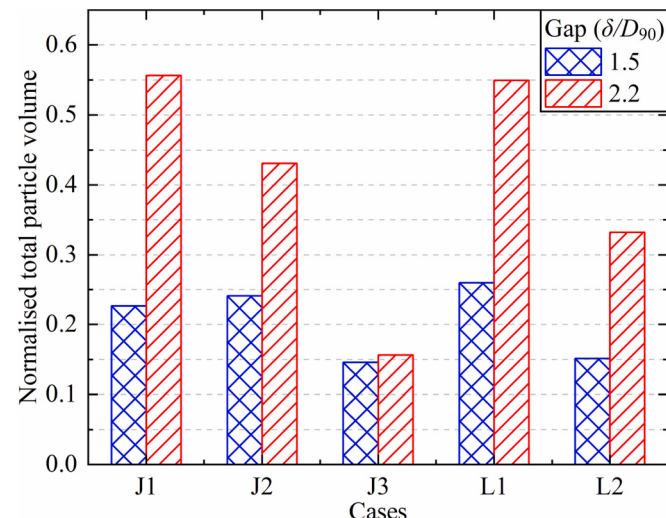
larger total particle volume of spread layer and less area ratio of empty patches. This is mainly due to that the jamming effect in case L1 is much smaller than that of case J1, as discussed in Section 3.1. This is clear evidence that powder spreadability is strongly affected by particle jamming.

As shown in Fig. 15, with the increase of cohesion number or the decrease of CY number, the trend of non-uniformity is similar to that of empty patches area and total particle volume. However, for the case of J1 at gap height of $\delta = 1.5D_{90}$, the value of SI is much larger than other cases at the same spreading conditions. It agrees well with the snapshots of spread layer in Fig. 12, where the particles are pushed together while
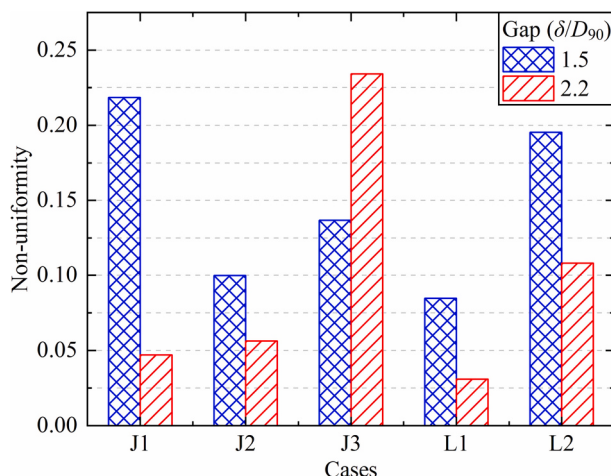
Fig. 15. Non-uniformity of the spread layer.

several long empty patches could be found. This is mainly due to the jamming effect, which agrees well with Fig. 6. Correspondingly, the uniformity of case L1 is better than that of case J1. The data in Figs. 13–15 all shows that case L1 has the best spreadability at both gap heights, i.e. smallest empty patches area and non-uniformity, largest total particle volume. This is mainly due to that particles in case L1 have less jamming around the gap and better flowability within the heap. Therefore, the spreadability is strongly affected by the plastic deformation of particles.

4. Conclusion

In this work, the effect of plastic deformation on the spreadability of cohesive powder is detailed investigated. Particle jamming, particle dynamics within the heap, and the quality of spread layer is analysed. The main results highlight the importance of plastic deformation on spreadability, which are summarised as follows:

1) Mechanical jamming at narrow gap is significantly reduced by the effect of plastic deformation. There are almost no burst particles and the blade force is weak when considering plastic deformation. The strength of mechanical jamming could be enhanced by large cohesion of particles.
2) Under the effect of plastic deformation, the flowability of particles within the heap becomes worse, even making the particles be dragged by the blade as a block. Large tensile force of particle-particle contacts could be induced by jamming even when CY number is larger than 1. The tensile force usually has larger value in the region close to the blade, and it could be 100 times of the value predicted by JKR theory.
3) Effects of plastic deformation on powder spreadability could not be simply replaced by increasing the surface energy of particles. Better spreadability could be obtained if the effect of the plastic deformation is considered due to less jamming. However, if the plastic deformation of particles within the heap is too large, spreadability would be significantly reduced due to worse flowability.

CRediT authorship contribution statement

Wenguang Nan: Conceptualization, Investigation, Writing – original draft, Writing – review & editing. **Md Arifur Rahman:** Investigation, Writing – original draft. **Lanzhou Ge:** Writing – original draft, Writing – review & editing. **Zhonggang Sun:** Writing – review & editing.

Declaration of Competing Interest

The authors declare that they have no known competing financial interests or personal relationships that could have appeared to influence the work reported in this paper.

Data availability

Data will be made available on request.

References

[1] T.D. Ngo, A. Kashani, G. Imbalzano, K.T.Q. Nguyen, D. Hui, Additive manufacturing (3D printing): a review of materials, methods, applications and challenges, Compos. Part B 143 (2018) 172–196.
[2] W.S.W. Harun, M.S.I.N. Kamariah, N. Muhamad, S.A.C. Ghani, F. Ahmad, Z. Mohamed, A review of powder additive manufacturing processes for metallic biomaterials, Powder Technol. 327 (2018) 128–151.
[3] W.E. Frazier, Metal additive manufacturing: a review, J. Mater. Eng. Perform. 23 (2014) 1917–1928.
[4] N. Guo, M.C. Leu, Additive manufacturing: technology, applications and research needs, Front. Mech. Eng. 8 (2013) 215–243.
[5] N. Shamsaei, A. Yadollahi, L. Bian, S.M. Thompson, An overview of Direct Laser Deposition for additive manufacturing; Part II: Mechanical behavior, process parameter optimization and control, Addit. Manuf. 8 (2015) 12–35.
[6] S. Singh, S. Ramakrishna, R. Singh, Material issues in additive manufacturing: a review, J. Manuf. Process. 25 (2017) 185–200.
[7] I. Gibson, D. Rosen, B. Stucker, Additive Manufacturing Technologies, 3D Printing, Rapid Prototyping, and Direct Digital Manufacturing, Springer, New York, 2015.
[8] J. Zhang, Y. Tan, T. Bao, Y. Xu, X. Xiao, S. Jiang, Discrete element simulation of the effect of roller-spreading parameters on powder-bed density in additive manufacturing, Materials 13 (2020) 2285.
[9] S. Wu, Z. Lei, M. Jiang, J. Liang, B. Li, Y. Chen, Experimental investigation and discrete element modeling for particle-scale powder spreading dynamics in powder-bed-fusion-based additive manufacturing, Powder Technol. 403 (2022) 117390.
[10] L. Si, T. Zhang, M. Zhou, M. Li, Y. Zhang, H. Zhou, Numerical simulation of the flow behavior and powder spreading mechanism in powder bed-based additive manufacturing, Powder Technol. 394 (2021) 1004–1016.
[11] A. Townsend, N. Senin, L. Blunt, R.K. Leach, J.S. Taylor, Surface texture metrology for metal additive manufacturing: a review, Precis. Eng. 46 (2016) 34–47.
[12] P. Bidare, R.R.J. Maier, R.J. Beck, J.D. Shephard, A.J. Moore, An open-architecture metal powder bed fusion system for in-situ process measurements, Add. Manufact. 16 (2017) 177–185.
[13] W. Nan, M. Pasha, T. Bonakdar, A. Lopez, U. Zafar, S. Nadimi, M. Ghadiri, Jamming during particle spreading in additive manufacturing, Powder Technol. 338 (2018) 253–262.
[14] M. Ghadiri, M. Pasha, W. Nan, C. Hare, V. Vivacqua, U. Zafar, S. Nezamabadi, A. Lopez, M. Pasha, S. Nadimi, Cohesive powder flow: trends and challenges in characterisation and analysis, KONA Powder Par. J. 37 (2020) 3–18.
[15] M. Ahmed, M. Pasha, W. Nan, M. Ghadiri, A simple method for assessing powder spreadability for additive manufacturing, Powder Technol. 367 (2020) 671–679.
[16] G. Craft, J. Nussbaum, N. Crane, J.P. Harmon, Impact of extended sintering times on mechanical properties in PA-12 parts produced by powderbed fusion processes, Add. Manufact. 22 (2018) 800–806.
[17] D. Nasato, T. Pöschel, Influence of particle shape in additive manufacturing: discrete element simulations of polyamide 11 and polyamide 12 (36) (2020) 101421.
[18] D. Schiochet Nasato, H. Briesen, T. Pöschel, Influence of vibrating recoating mechanism for the deposition of powders in additive manufacturing: discrete element simulations of polyamide 12, Add. Manufact. 48 (2021) 102248.
[19] Y. Wang, Z. Xu, D. Wu, J. Bai, Current status and prospects of polymer powder 3D printing technologies, Materials 13 (2020).
[20] M.Y. Shaheen, A.R. Thornton, S. Luding, T. Weinhart, The influence of material and process parameters on powder spreading in additive manufacturing, Powder Technol. 383 (2021) 564–583.
[21] D. Yao, X. An, H. Fu, H. Zhang, X. Yang, Q. Zou, K. Dong, Dynamic investigation on the powder spreading during selective laser melting additive manufacturing, Add. Manufact. 37 (2021) 101707.
[22] V.V. Ganesan, A. Amerinatanzi, A. Jain, Discrete element modeling (DEM) simulations of powder bed densification using horizontal compactors in metal additive manufacturing, Powder Technol. 405 (2022) 117557.

[23] L. Wang, A. Yu, E. Li, H. Shen, Z. Zhou, Effects of spreader geometry on powder spreading process in powder bed additive manufacturing, Powder Technol. 384 (2021) 211–222.

[24] A. Phua, C. Doblin, P. Owen, C.H.J. Davies, G.W. Delaney, The effect of recoater geometry and speed on granular convection and size segregation in powder bed fusion, Powder Technol. 394 (2021) 632–644.

[25] Z. Snow, R. Martukanitz, S. Joshi, On the development of powder spreadability metrics and feedstock requirements for powder bed fusion additive manufacturing, Addit. Manuf. 28 (2019) 78–86.

[26] E.J.R. Parteli, T. Pöschel, Particle-based simulation of powder application in additive manufacturing, Powder Technol. 288 (2016) 96–102.

[27] S. Haeri, Y. Wang, O. Ghita, J. Sun, Discrete element simulation and experimental study of powder spreading process in additive manufacturing, Powder Technol. 306 (2017) 45–54.

[28] D. Yao, X. Liu, J. Wang, W. Fan, M. Li, H. Fu, H. Zhang, X. Yang, Q. Zou, X. An, Numerical insights on the spreading of practical 316 L stainless steel powder in SLM additive manufacturing, Powder Technol. 390 (2021) 197–208.

[29] H. Chen, Q. Wei, S. Wen, Z. Li, Y. Shi, Flow behavior of powder particles in layering process of selective laser melting: numerical modeling and experimental verification based on discrete element method, Int. J. Mach. Tools Manuf. 123 (2017) 146–159.

[30] H. Chen, Q. Wei, Y. Zhang, F. Chen, Y. Shi, W. Yan, Powder-spreading mechanisms in powder-bed-based additive manufacturing: experiments and computational modeling, Acta Mater. 179 (2019) 158–171.

[31] A. Mussatto, R. Groarke, A. O'Neill, M.A. Obeidi, Y. Delaure, D. Brabazon, Influences of powder morphology and spreading parameters on the powder bed topography uniformity in powder bed fusion metal additive manufacturing, Add. Manufact. 38 (2021).

[32] T.-P. Le, X. Wang, K.P. Davidson, J.E. Fronda, M. Seita, Experimental analysis of powder layer quality as a function of feedstock and recoating strategies, Add. Manufact. 39 (2021).

[33] J. Zhang, Y. Tan, X. Xiao, S. Jiang, Comparison of roller-spreading and blade-spreading processes in powder-bed additive manufacturing by DEM simulations, Particuology 66 (2022) 48–58.

[34] Y. He, A. Hassanpour, A.E. Bayly, Combined effect of particle size and surface cohesiveness on powder spreadability for additive manufacturing, Powder Technol. 392 (2021) 191–203.

[35] W. Nan, W.P. Goh, M.T. Rahman, Elasto-plastic and adhesive contact: An improved linear model and its application, Powder Technol. 407 (2022) 117634.

[36] C. Thornton, Granular Dynamics, Contact Mechanics and Particle System Simulations: A DEM Study, 2015.

[37] P.A. Cundall, O.D.L. Strack, A discrete numerical model for granular assemblies, Geotechnique 29 (1979) 47–65.

[38] K.L. Johnson, K. Kendall, A.D. Roberts, D. Tabor, Surface energy and the contact of elastic solids, Proc. Royal Soc. London. A. Math. Phys. Sci. 324 (1971) 301–313.

[39] W.G. Nan, M. Ghadiri, Numerical simulation of powder flow during spreading in additive manufacturing, Powder Technol. 342 (2019) 801–807.

[40] C. Thornton, Granular Dynamics, Contact Mechanics and Particle System Simulations: A DEM Study, 2015.

[41] W. Nan, M. Pasha, M. Ghadiri, Numerical simulation of particle flow and segregation during roller spreading process in additive manufacturing, Powder Technol. 364 (2020) 811–821.

[42] W. Nan, Y. Gu, Experimental investigation on the spreadability of cohesive and frictional powder, Adv. Powder Technol. 33 (2022).